



*Geochemistry, Geophysics, Geosystems*

Supporting Information for

**Slab temperature evolution over the lifetime of a subduction zone**

Adam F. Holt<sup>1</sup> and Cailey B. Condit<sup>2</sup>

1: Rosenstiel School of Marine and Atmospheric Science, University of Miami, FL

2: Department of Earth and Space Sciences, University of Washington, Seattle, WA

**Contents of this file**

Figures S1 to S13

Text S1

Tables S1 to S3

**Additional Supporting Information (Files uploaded separately)**

Captions for Dataset S1

**Introduction**

This supplementary document contains additional figures relating to both numerical and thermodynamic modeling components on the manuscript. We also provide an overview of the thermodynamic modeling approach (Text S1) and thermodynamic calculation parameters (Tables S1-S3).

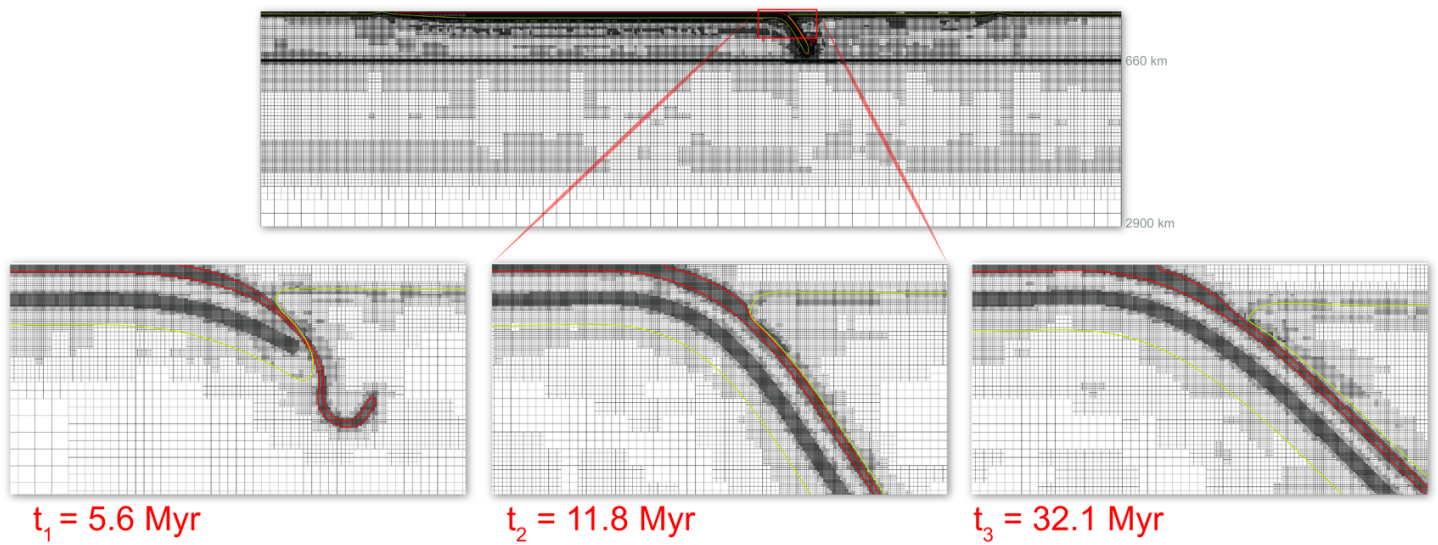


**Figure S1.** Computational mesh of the reference model. The three snapshots correspond to those of main text Figure 1. The red contour outlines the crust and the yellow contour is the 1000 °C isotherm.

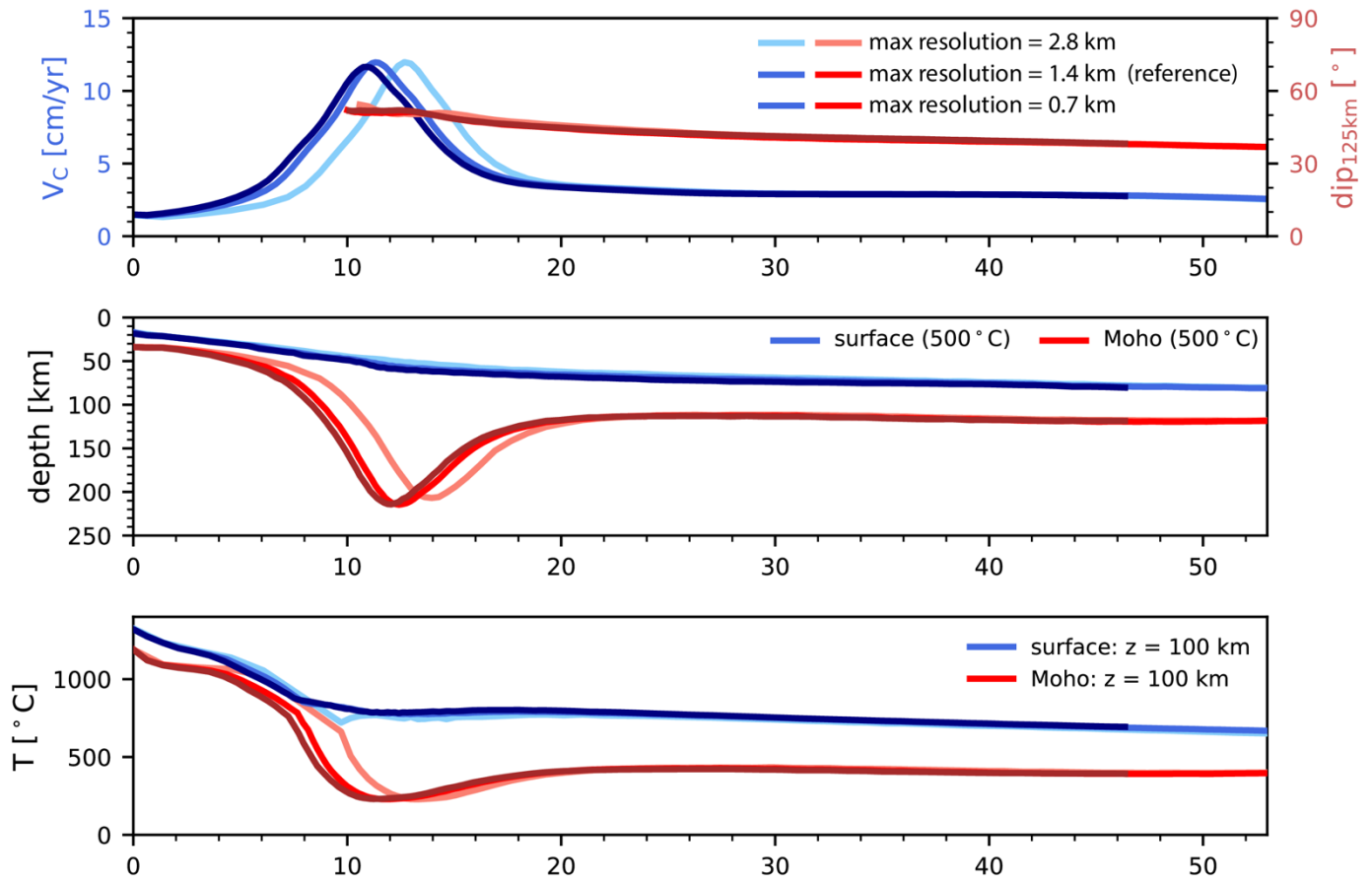


**Figure S2.** Time dependent subduction kinematics and slab temperature as a function of mesh resolution. Higher (minimum element size = 0.7 km) and lower resolution (min. element size = 2.8 km) models tested relative to the reference model (min. element size = 1.4 km). Quantities plotted are equivalent to those of main text Figure 2.

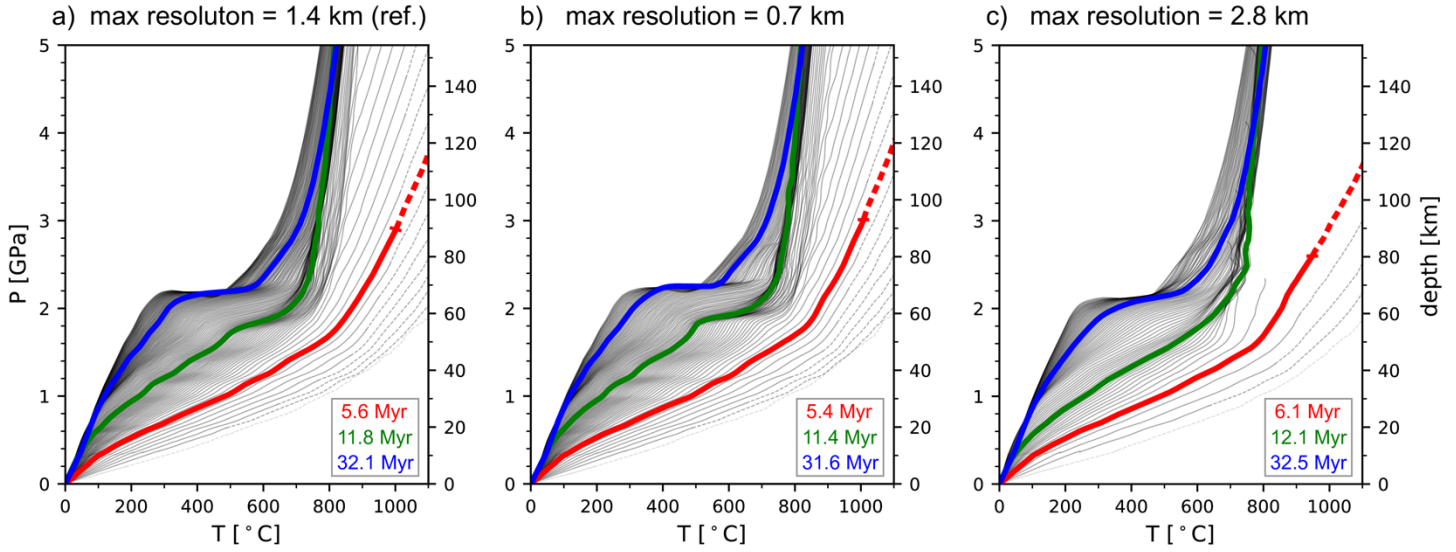


**Figure S3.** Time dependent slab top pressure-temperature conditions as a function of mesh resolution. Higher (minimum element size = 0.7 km) and lower resolution (min. element size = 2.8 km) models tested relative to the reference model (min. element size = 1.4 km). Quantities plotted are equivalent to those of main text Figure 6. The first, faint profile corresponds to  $t = 0$  (i.e., the initial conditions), and we dash profiles at depths greater than those that an initially flat-lying crust would reach.

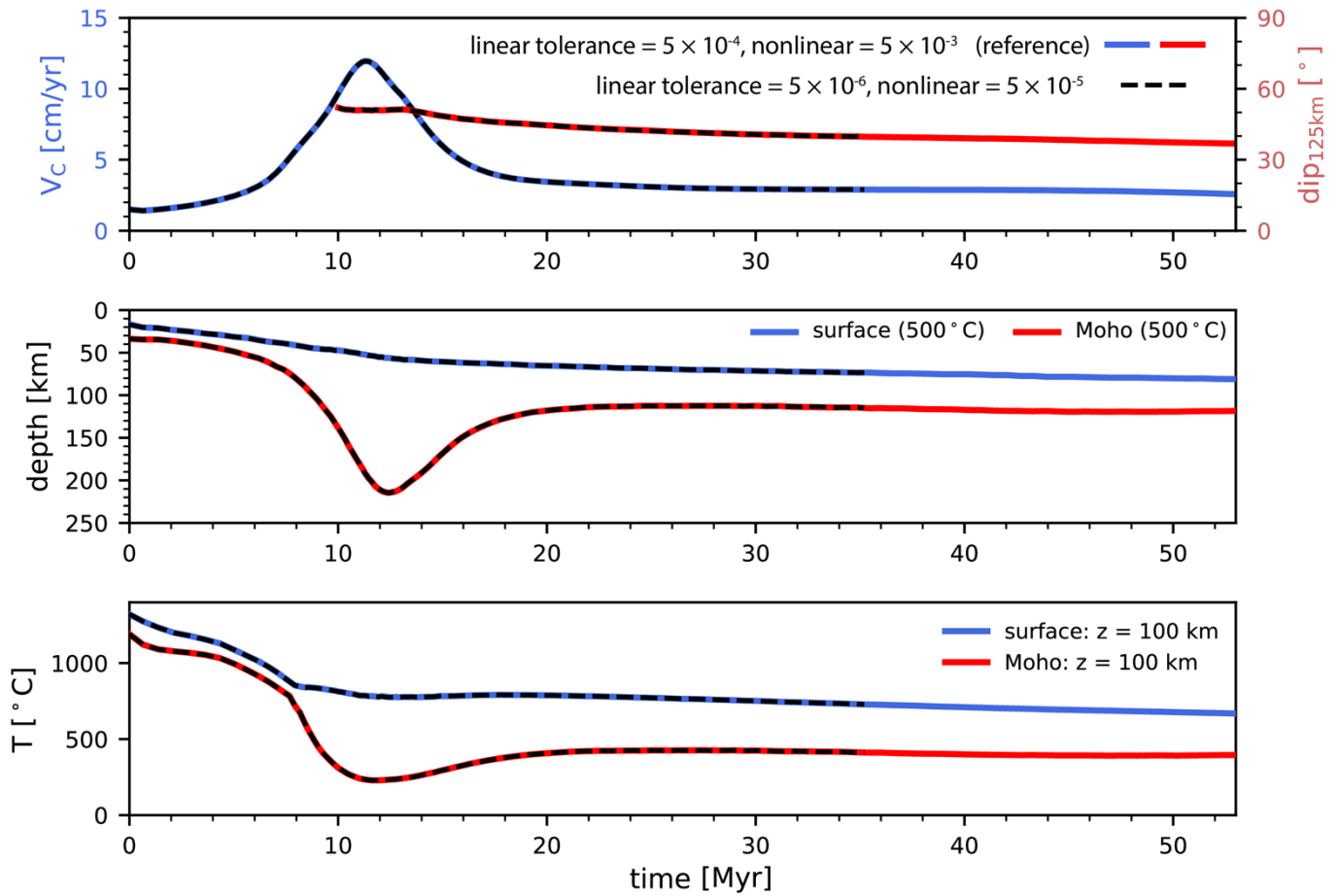


**Figure S4.** Time dependent subduction kinematics and slab temperature as a function of numerical accuracy. Stricter numerical tolerances are examined relative to the reference. Quantities plotted are equivalent to those of main text Figure 2.

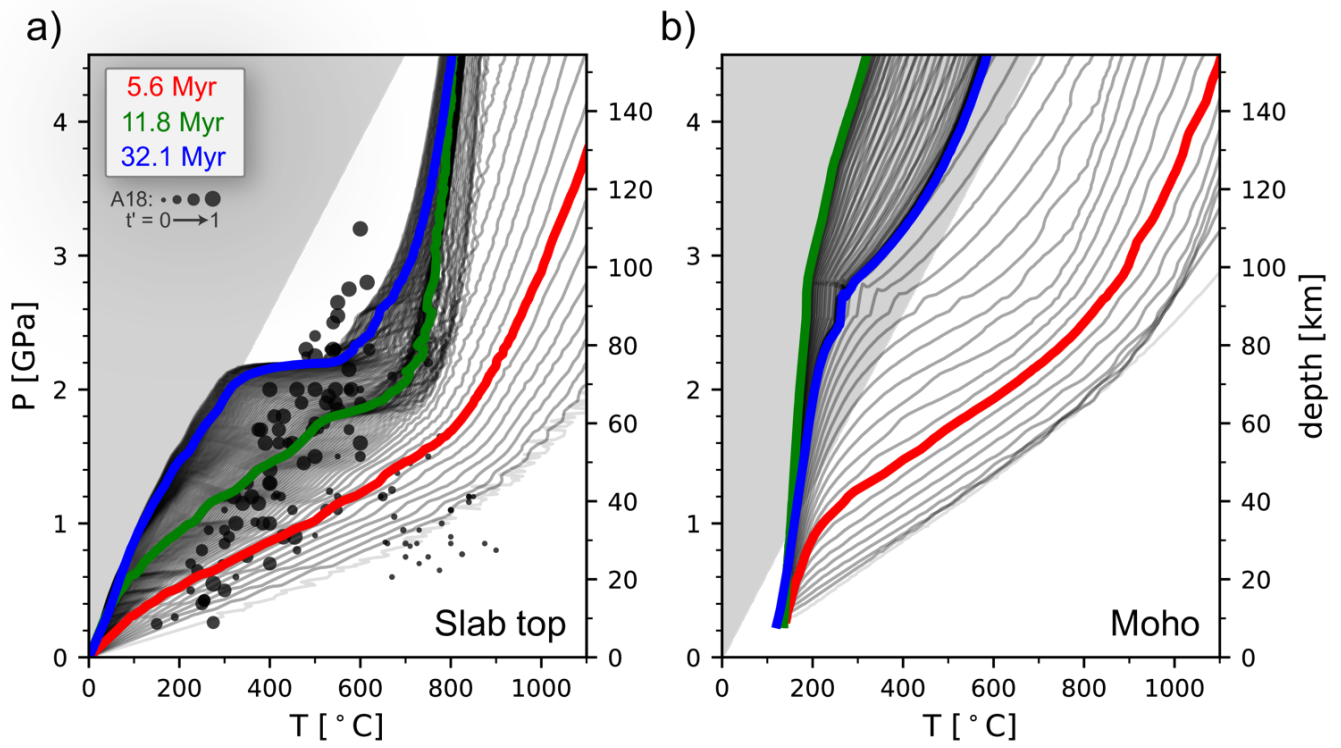


**Figure S5.** Raw (i.e., unsmoothed) slab top and slab Moho P-T evolution of the reference model. Equivalent to main text Figure 3 but without the smoothing post-processing step and additional overlays. The first, faint profile corresponds to  $t = 0$  (i.e., the initial conditions).

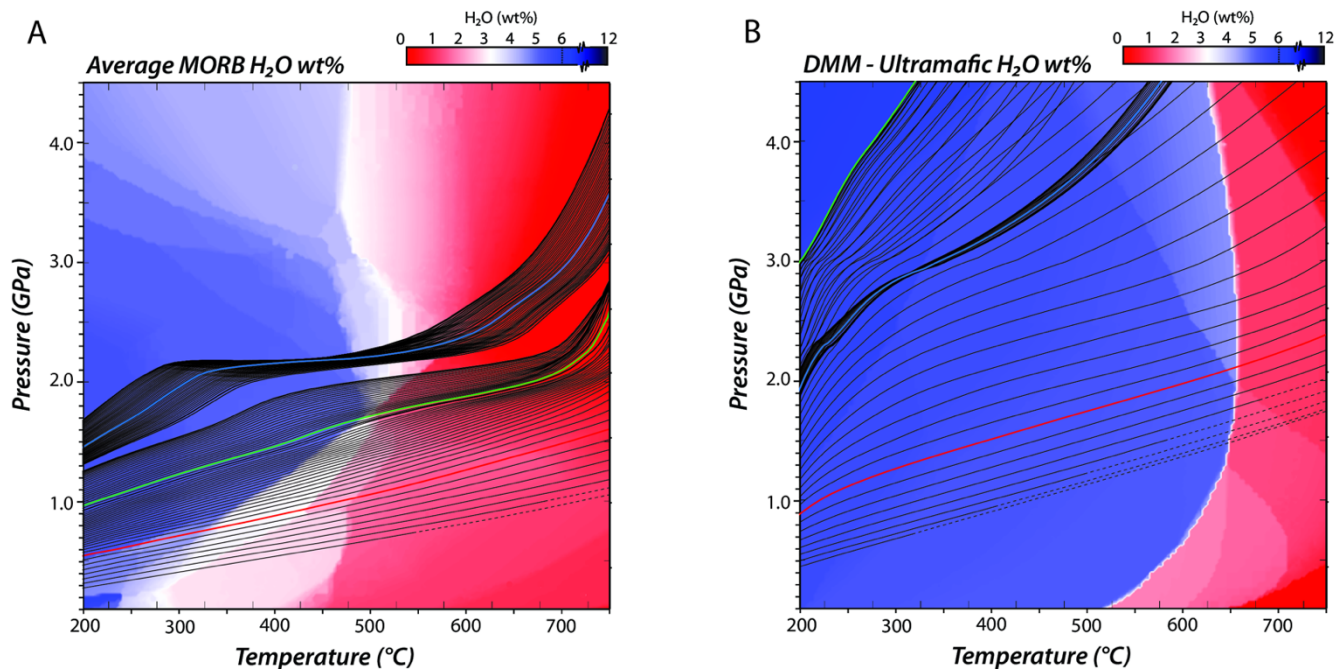


**Figure S6.** Mineral bound water surfaces over  $P$ - $T$  space for (A) MORB and (B) DMM.  $P$ - $T$  paths in (A) are interpolated slab top paths from the strong crust geodynamic model plotted every  $\sim 1$  Myr, while  $P$ - $T$  paths in (B) are for the slab Moho plotted every  $\sim 0.5$  Myr. Bolded red lines represent subduction *initiation* phase, green line represents *free sinking* phase, and blue line represents *mature* phase of subduction. We dash the profiles at lithostatic pressures greater than that which an initially flat-lying crust would reach.

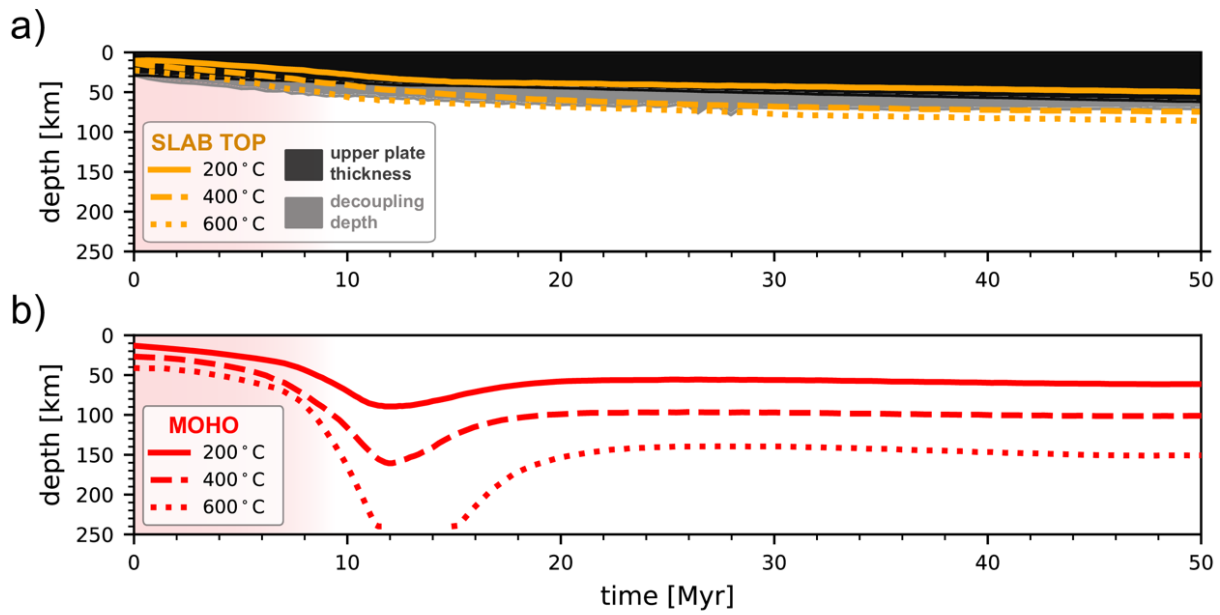


**Figure S7.** Time dependent slab temperature evolution of the reference model. Similar to main text Figure 2 (Panels B and C), but with additional temperatures and depths extracted from the slab top and slab Moho.

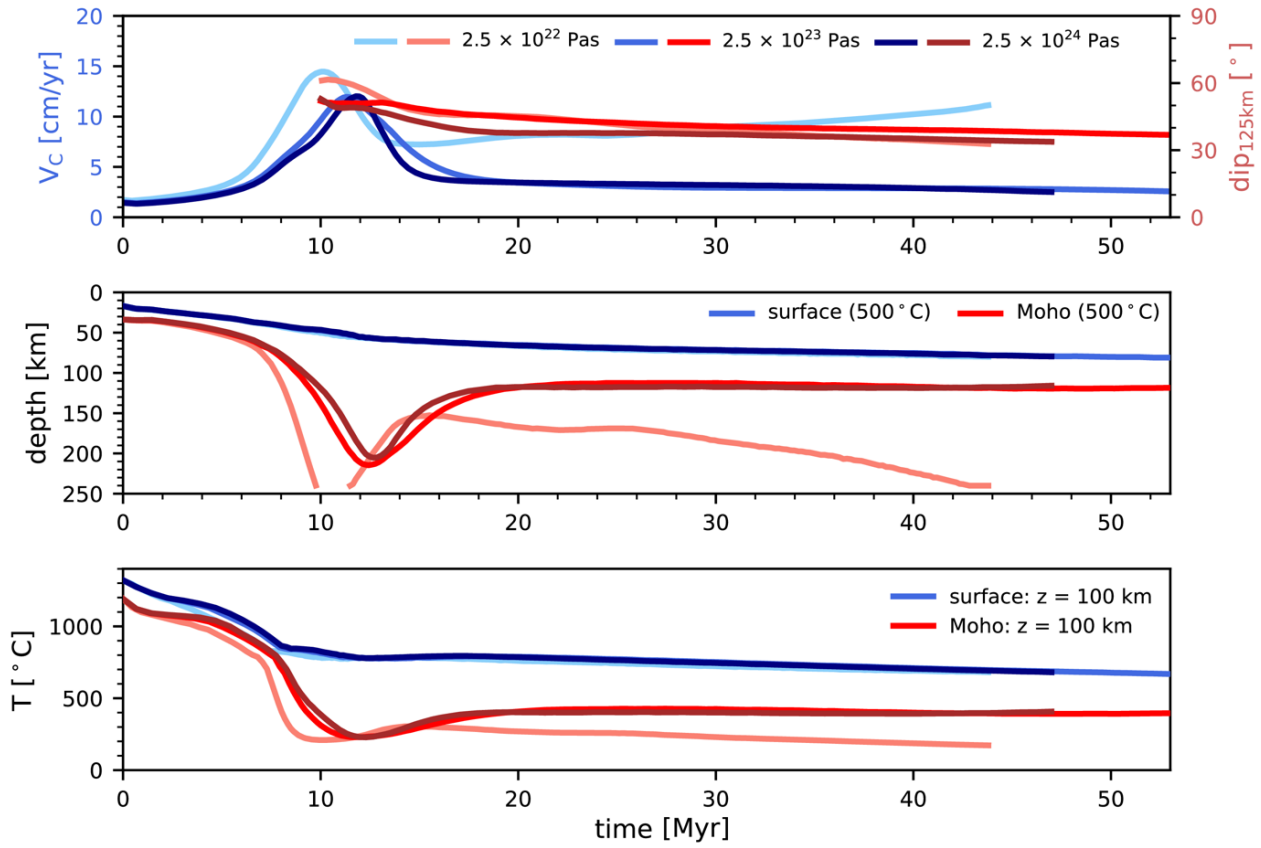


**Figure S8.** Time dependent subduction kinematics and slab temperature as a function of slab viscosity. Stronger ( $2.5 \times 10^{24}$  Pa s) and weaker slabs ( $2.5 \times 10^{22}$  Pa s) tested relative to the reference ( $2.5 \times 10^{23}$  Pa s). Quantities plotted are equivalent to those of main text Figure 2.

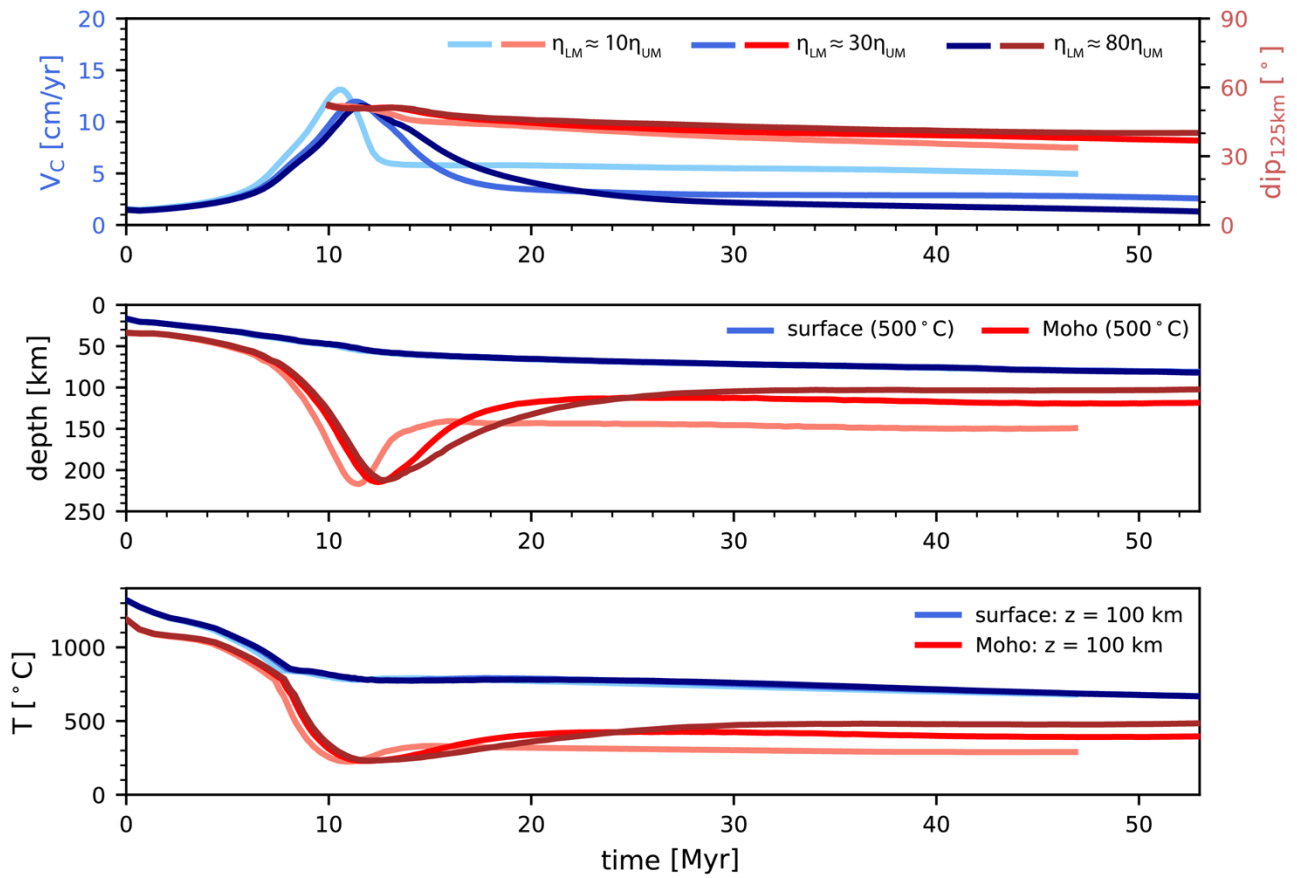


**Figure S9.** Time dependent subduction kinematics and slab temperature as a function of lower mantle viscosity. Note that time-dependent dislocation creep activation produces a time dependent upper-to-lower mantle viscosity ratio. The quoted viscosity contrasts ( $\eta_{LM}/\eta_{UM} \approx 10, 30, 80$ ) are average values during the mature phase of subduction. Quantities plotted are equivalent to those of main text Figure 2.

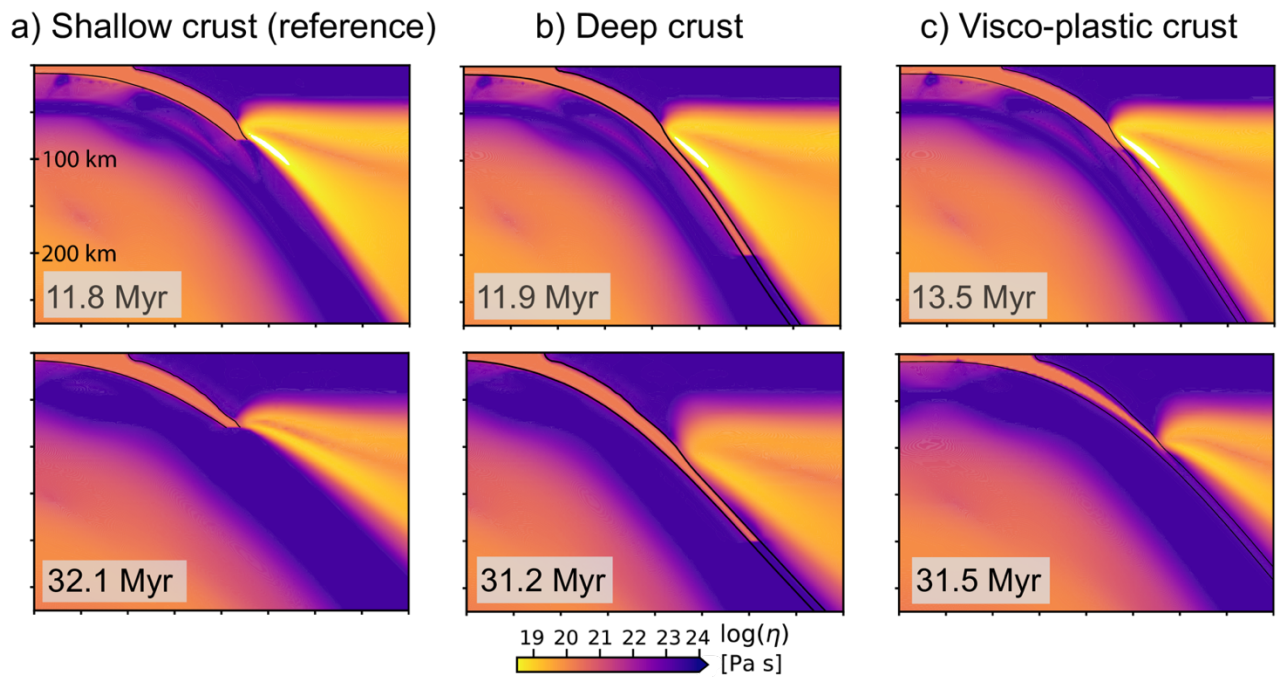


**Figure S10.** Near-trench viscosity field as a function of crustal parameterization. Relative to the reference (80 km depth crust cut-off), deeper cut-off depth (200 km depth crust cut-off) and visco-plastic crust cases are examined. Panels are equivalent to those of main text Figure 6 but enlarged and without additional (non-viscosity field) annotations.

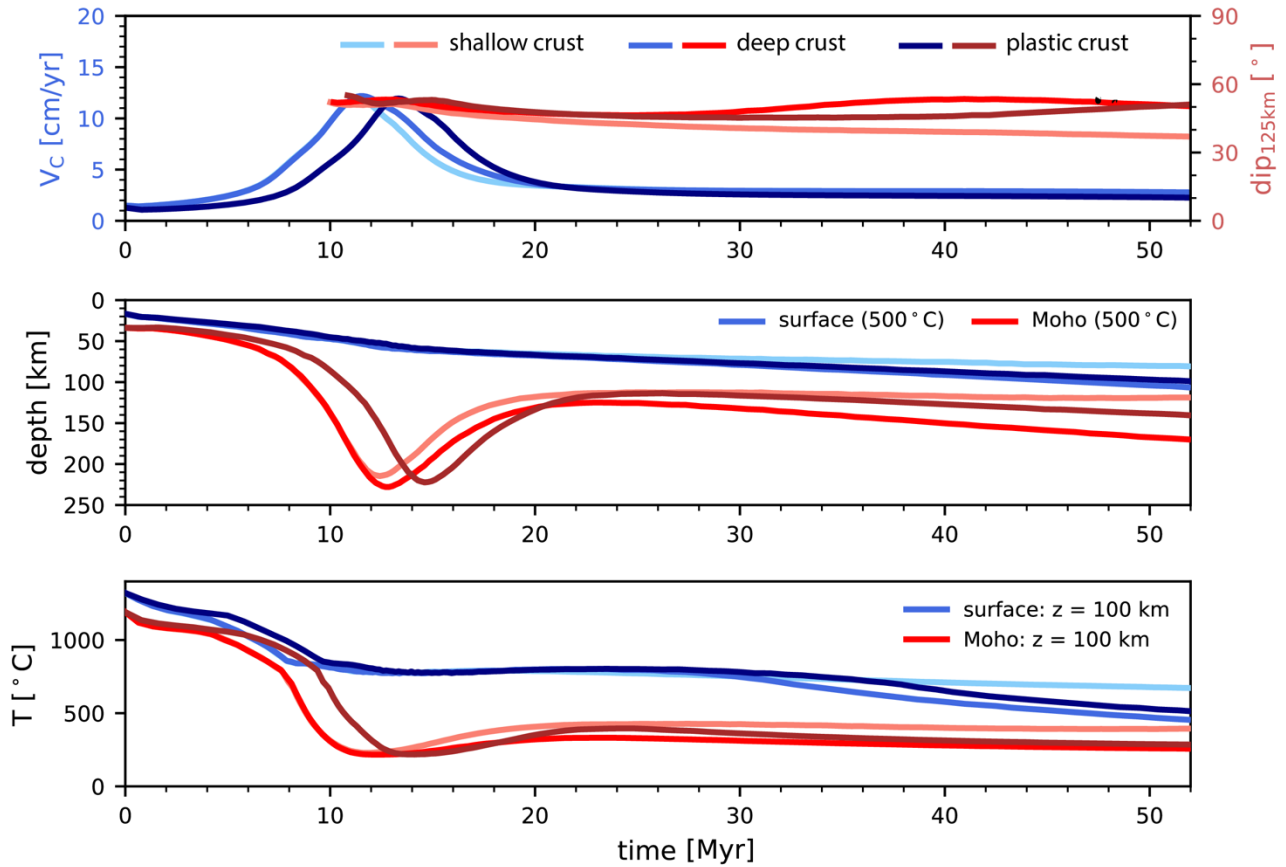


**Figure S11.** Crustal parametrization tests. Time dependent subduction kinematics and slab temperature as a function of crustal parameterization. Relative to the reference (80 km depth crust cut-off), deeper cut-off depth (200 km depth crust cut-off) and visco-plastic crust cases are examined. Quantities plotted are equivalent to those of main text Figure 2.

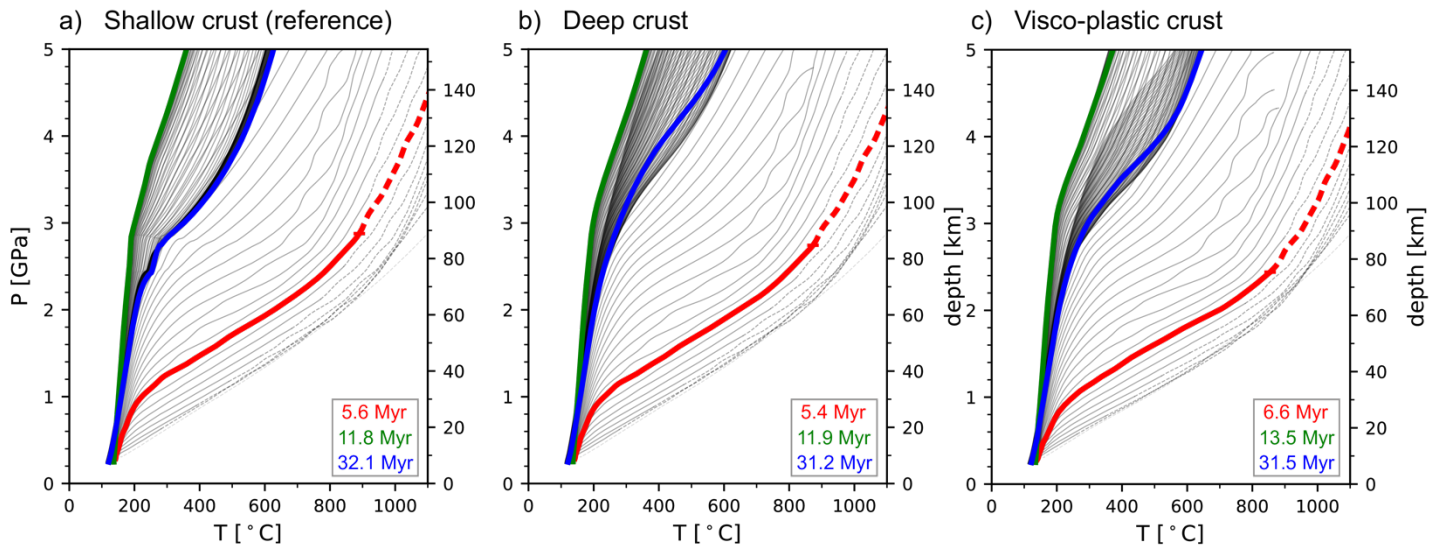


**Figure S12.** Slab Moho  $P$ - $T$  evolution as a function of crustal parameterization. Equivalent to main text Figure 6 but with Moho instead of slab Moho  $P$ - $T$ . The first, faint profile corresponds to  $t = 0$  (i.e., the initial conditions), and we dash profiles at depths greater than that which an initially flat-lying crust would reach.

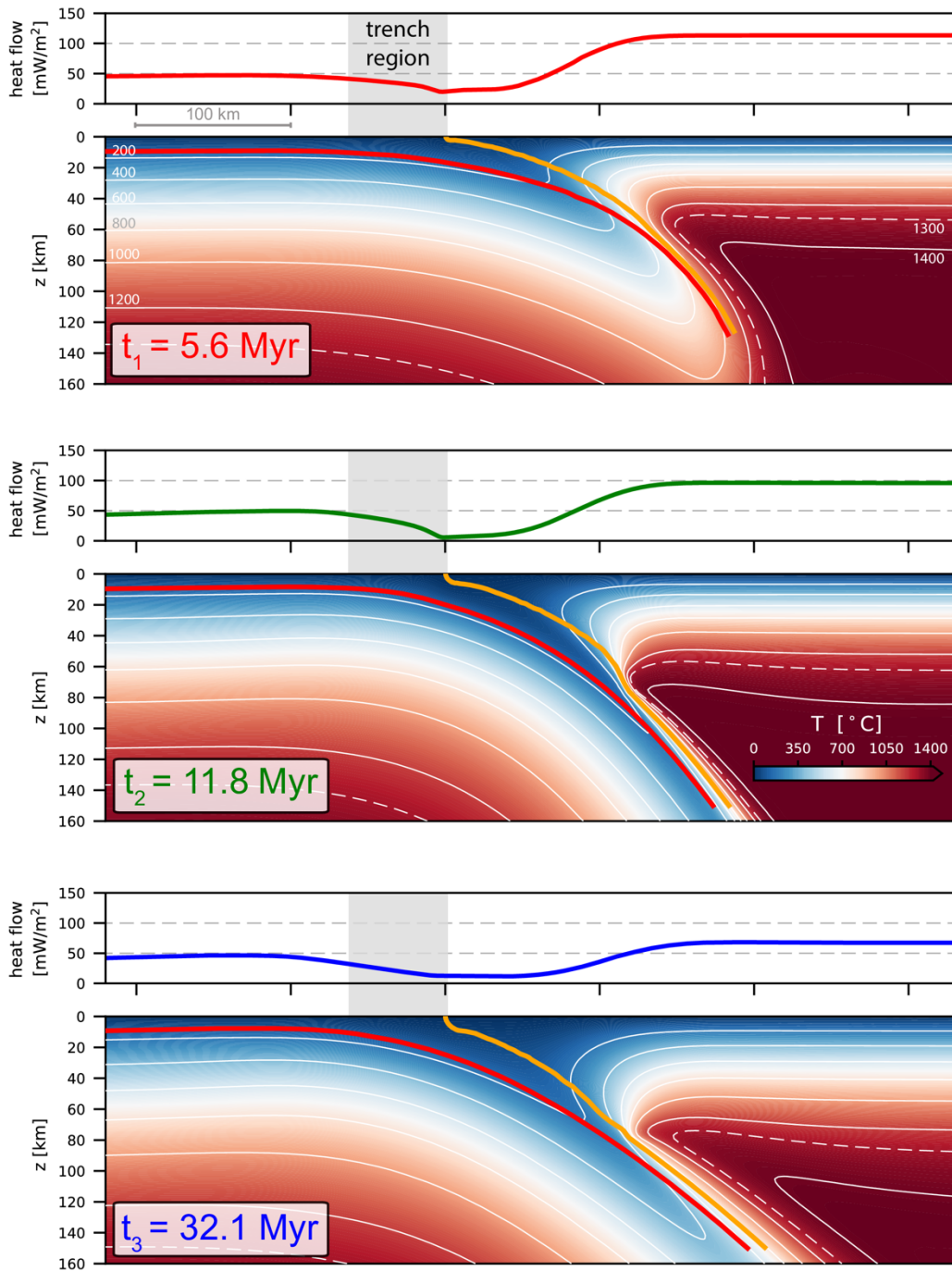


**Figure S13:** Surface heat flow evolution of the reference models. Zoomed in to the trench region, model temperature and surface heat flow are plotted for the three time-steps shown in Figure 1.

## Text S1: Details of Thermodynamic Phase Equilibria Modeling

### *Bulk rock compositions*

We modeled two lithologies from subducting oceanic lithosphere to evaluate dehydration reactions along the evolving plate interface and slab Moho: average MORB from Gale et al., [2013] and depleted MORB mantle peridotite from Miyashiro et al. [1969]. The average MORB composition is the geometric mean MORB from Gale et al. [2013], with Fe<sub>2</sub>O<sub>3</sub> calculated from total FeO using the Fe<sup>3+</sup>/Fe<sub>total</sub> ratio of 0.16 from Cottrell and Kelley [2011].

	Average MORB	Depleted MORB Mantle
SiO <sub>2</sub>	50.69	40.58
TiO <sub>2</sub>	1.69	-
Al <sub>2</sub> O <sub>3</sub>	14.76	2.86
Fe <sub>2</sub> O <sub>3</sub>	1.86	4.69
FeO	8.80	3.43
MgO	7.61	33.2
CaO	11.44	2.05
Na <sub>2</sub> O	2.80	-
K <sub>2</sub> O	0.16	-

**Table S1:** Bulk rock compositions in wt% used in phase equilibria modeling.

### *P-T space, model systems, thermodynamic datasets, and solution models used*

Phase Assemblage Diagrams (pseudosections) were constructed for each bulk composition in Table S1 over pressure and temperature ranges of 0.1-4.5 GPa and 200-750 °C. The model system used was Na<sub>2</sub>O-CaO-K<sub>2</sub>O-FeO-MgO-Al<sub>2</sub>O<sub>3</sub>-SiO<sub>2</sub>-H<sub>2</sub>O-TiO<sub>2</sub>-O<sub>2</sub> for MORB. The depleted MORB mantle peridotite was modelled in the same system without K<sub>2</sub>O, and Na<sub>2</sub>O. We used the internally-consistent thermodynamic dataset of Holland and Powell [2011] (THERMOCALC

ds62) and corresponding solution models (shown below in Table S2) for MORB. For depleted MORB mantle peridotite, we used a 2004 update of the Holland and Powell [1998] thermodynamic dataset (THERMOCALC ds5.5) and corresponding solution models (shown in Table S3). H<sub>2</sub>O was considered a saturated fluid phase using a modified Redlich-Kwong fluid equation of state from Holland and Powell [1991].

Solution Phase	Solution Model
Biotite	Bi (W)
Brucite	B
Chlorite	Chl(W)
Chloritoid	Ctd(W)
Epidote	Ep(HP11)
Garnet	Gt(W)
Clinoamphibole	cAmph(G)
Orthopyroxene	Opx(W)
Clinopyroxene	Omph(GHP)
Antigorite	Atg(PN)
Spinel	Sp(WPC)
Olivine	O(HP)
Ilmenite	Ilm(WPH)
Ternary Feldspar	feldspar
Muscovite	Mica(W)

**Table S2:** Solution models considered in phase equilibria modelling for average MORB,

Solution Phase	Solution Model
Brucite	B
Carpholite	Carp
Chlorite	Chl(HP)
Chloritoid	Ctd(HP)
Epidote	Ep(HP)
Garnet	Gt(WPH)
Sudoite	Sud
Clinoamphibole	cAmph(DP)
Pumpellyite	Pu(M)
Orthopyroxene	Opx(HP)
Clinopyroxene	Omph(GHP)
Antigorite	Atg(PN)
Spinel	Sp(WPC)
Stilpnomelane	Stlp
Olivine	O(HP)
Ilmenite	Ilm(WPH)

**Table S3:** Solution models considered in phase equilibria modelling for depleted MORB mantle peridotite.

### **Dataset S1: ASPECT subduction model files**

Input files for all of the presented models.

## References

- Cottrell, E., and K. A. Kelley (2011), The oxidation state of Fe in MORB glasses and the oxygen fugacity of the upper mantle, *Earth Planet. Sci. Lett.*, 305(3–4), 270–282, doi:10.1016/j.epsl.2011.03.014.
- Gale, A., C. A. Dalton, C. H. Langmuir, Y. Su, and J. G. Schilling (2013), The mean composition of ocean ridge basalts, *Geochemistry, Geophys. Geosystems*, 14(3), 489–518, doi:10.1029/2012GC004334.
- Holland, T., and R. Powell (1991), A Compensated-Redlich-Kwong (CORK) equation for volumes and fugacities of CO<sub>2</sub> and H<sub>2</sub>O in the range 1 bar to 50 kbar and 100–1600°C, *Contrib. to Mineral. Petrol.*, 109(2), 265–273, doi:10.1007/BF00306484.
- Holland, T., and R. Powell (1998), An internally consistent thermodynamic data set for phases of petrological interest, *J. Met.*, 16, 309–343.
- Holland, T. J. B., and R. Powell (2011), An improved and extended internally consistent thermodynamic dataset for phases of petrological interest, involving a new equation of state for solids, *J. Metamorph. Geol.*, 29(3), 333–383, doi:10.1111/j.1525-1314.2010.00923.x.
- Miyashiro, A., F. Shido, and M. Ewing (1969), Composition and origin of serpentinites from the Mid-Atlantic Ridge near 24° and 30° North Latitude, *Contrib. to Mineral. Petrol.*, 23(2), 117–127, doi:10.1007/BF00375173.